IET Microwaves, Antennas & Propagation

Research Article

IET Journals
The Institution of Engineering and Technology

RCS reduction of microstrip antenna using split square loop thin absorber

ISSN 1751-8725
Received on 7th April 2020
Revised 2nd July 2020
Accepted on 4th August 2020
E-First on 24th September 2020
doi: 10.1049/iet-map.2020.0347
www.ietdl.org

Priyanka Das[1] ✉, *Kaushik Mandal*[2]

[1]*ECE, University of Engineering and Management, West Bengal, India*
[2]*Institute of Radio Physics and Electronics, University of Calcutta, West Bengal, India*
✉ *E-mail: priyankadas131986@gmail.com*

Abstract: This study proposes an electrically thin frequency-selective surface-based microwave absorber without using resistive surface and lumped resistors to make it simple and inexpensive. The ground plane of the microstrip antenna (MSA) serves as the metallic back of the absorber. The top two layers of the proposed absorber are printed on both sides of the top FR4 sheet in a square annular ring form to encircle the square patch. Both simulations and measurements are carried out to obtain the scattering parameters, which are used to retrieve the absorption coefficient, relative permittivity (ε_r), and relative permeability (μ_r). An equivalent circuit model for the proposed absorber is constructed and validated. The absorption performance is insensitive to the angle of incidence (θ) up to 50°. The absorption mechanisms are studied based on the surface current distribution, electric field distribution, and constitutive parameters. The absorber is then integrated with an MSA operating at 4.2 GHz, which gives a maximum monostatic radar cross-section (RCS) reduction of 15 dB. Numerical and experimental results of the radiation performance and the RCS of the absorber integrated antenna structure have been presented. A very good agreement between simulation and measurement results is observed.

1 Introduction

The reduction of radar cross-section (RCS) of an antenna without compromising its radiation characteristics is a topic of immense research interest. Metamaterials are periodic or quasi-periodic, subwavelength metallic structures in which the electromagnetic (EM) material properties are derived from the shape, size, or periodicity of the structure rather than directly from the material composition. This important property allows metamaterials to be geometrically scaled so as to operate in any desired spectral range. Triple-band metamaterial absorbers have been designed using an outer circular metal ring with an inner Jerusalem cross [1] and circular fractal structure [2]. Metamaterial inspired double split serration ring structure [3] and split-ring-slot structure [4] have been used to achieve the multiband absorption. The RCS of a waveguide slot antenna is reduced by covering its perfect electric conductor ground plane by metamaterial absorber in [5]. In [6], a polarisation conversion metamaterial is used to reduce the RCS of an microstrip antenna (MSA) by controlling the polarisation of reflected waves. Lumped resistors loaded on a 2D array of conductive crossed dipoles [7] and double-square loops [8] are used for absorbing the incident EM waves. Multi-resonant gridded square frequency-selective surface (FSS) structures are used to obtain a quad-resonant absorber in [9]. Wideband RCS reduction of an MSA working at 2.5 GHz is achieved by replacing the solid metal ground with 2.5D FSS [10] and using an absorptive FSS-based radome [11] for out-of-band EM waves. Wideband absorption can be achieved by using multiple layers consisting of patch and ring resonators [12], slotted metal loops [13] or graphene-based non-periodic metallic patch [14]. A dual polarised [15] absorptive frequency-selective rasorber is constructed by meander line square loops with and without lumped resistors loaded on the substrate. A via-based absorptive FSS [16] exhibits absorption at 5.45 GHz. In [17], the matrix transformation method for reducing return loss from dielectric surfaces by loading them with FSS is described. Broadband microwave absorption can be obtained by embedding a resistive FSS over a grounded dielectric substrate [18] or sandwiching it between two layers of magnetic sheets [19]. A resistor free partially transmissible absorptive FSS [20] is described at 2.46 GHz. A combination of hexagonal-shaped artificial impedance surface and a resistor–capacitor-based metamaterial absorber is demonstrated in [21] for X-band applications. A single-layer circuit analogue absorber consisting of resistor-loaded double-square loop arrays [22] has been investigated. A bandwidth of 0.68 GHz is achieved by a periodic array (2×2) of the Swastika-like structure [23] printed on an FR4 dielectric substrate backed by copper ground. An air gap is incorporated between two RO4003 layers to realise a wideband circuit analogue absorber [24].

The use of absorbing ground plane for the antenna's RCS reduction often encounters two critical problems: narrow absorption bandwidth and degradation of radiation performance of the antenna. The fabrication of resistive surfaces which, is the key to design a wideband absorber, is not apt for lithographic techniques. Also, fabrication by screen printing incurs a high price. In this paper, the above-mentioned shortcomings are overcome by designing a metallic FSS-based absorber. This metallic backed absorber is designed without using any lumped resistors and resistive surface, which reduces fabrication cost and structural complexity, and also provides more degrees of freedom on pattern designing. It can be fabricated easily by using a commonly printed circuit board fabrication method. The proposed absorber exhibits a reflection coefficient (S_{11}) ≤ -10 dB from 4.9–7.5 GHz resulting in absorption of above 90% over a fractional bandwidth of 42%. This paper aims at reducing the RCS of MSA operating at 4.2 GHz by integrating it with the proposed absorber.

2 Design and analysis of the proposed absorber structure

The proposed absorber structure is designed on an FR-4 substrate, having relative permittivity (ε_r) of 4.4 and loss tangent ($\tan\delta$) of 0.02 having a thickness (h) of 3.2 mm. The absorber unit cell in Fig. 1 is a three-layered composite structure comprising of four symmetrical and identical sub-cells. Each sub-cell comprises a dog-bone-shaped resonator enclosed by a split-square loop resonator. The layout of both the first and second layers is identical. These two layers are printed on top and bottom sides of the 1.6 mm thick FR4 substrate. The bottom layer (metallic back)

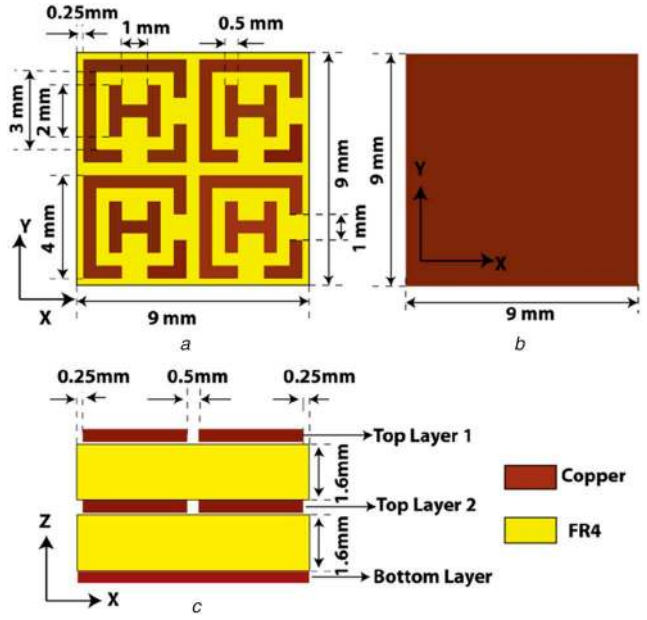

Fig. 1 *Unit cell geometry of the proposed FSS-based absorber*

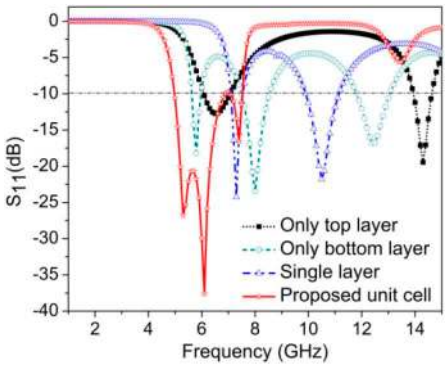

Fig. 2 *S_{11} characteristics in presence and absence of different layers*

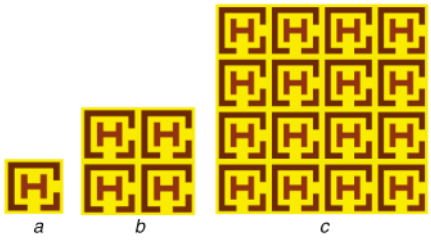

Fig. 3 *Geometries of the unit cell*
(a) 1-element, ***(b)*** 4-element (proposed), ***(c)*** 16-element

of the absorber is printed on the bottom of another FR4 sheet of the same thickness (1.6 mm). These two substrates are sandwiched to form the proposed structure of overall thickness 3.2 mm, which is equivalent to 0.052λ, where λ is the wavelength corresponding to the lowest frequency (4.9 GHz) of the absorption band. The absence of an air gap between the consecutive FSS layers aids in compactness and miniaturisation of the absorber. The absorber was simulated and optimised using the finite element method (FEM)-based Ansys® HFSS^{TM} EM simulator. The periodic boundary conditions and floquet ports are utilised to simulate the infinite periodic cells.

The proposed absorber consists of a high impedance surface comprising four identical metallic elements on both the top and bottom sides of the FR4 substrate. If only the top layer is present, the absorber exhibits narrow impedance ($S_{11} \leq -10$ dB) bandwidth from 6.1 to 7 GHz, as seen in Fig. 2. If only the bottom layer is present, the absorber exhibits dual-band absorption at 5.8 and 8 GHz. If the absorber is single layered having a thickness of 1.6

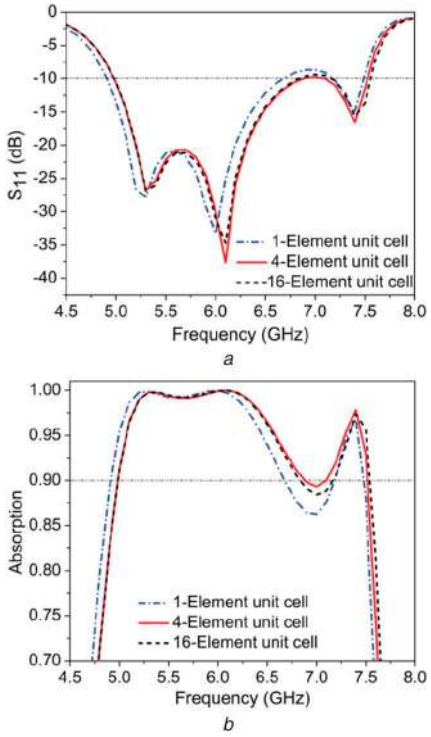

Fig. 4 *Performance comparison of 1-element, 4-element (proposed), and 16-element unit cell*
(a) Reflection coefficient, ***(b)*** Absorption

mm, matching of impedance takes place at 7.3 and 10.5 GHz, as shown in Fig. 2. The proposed unit cell with both the top and bottom layers is therefore chosen because it gives a wide bandwidth (4.9–7.5 GHz) with maximum absorption at 6.1 GHz.

The performances of the proposed unit cell (9 mm × 9 mm) having four identical elements (Fig. 3*b*), one-quarter of the proposed unit cell (4.5 mm × 4.5 mm) (Fig. 3*a*), and 16-element unit cell (18 mm × 18 mm) (Fig. 3*c*) are compared in terms of the reflection coefficient (Fig. 4*a*) and absorption (Fig. 4*b*). In Fig. 4*a*, the reflection coefficient (S_{11}) of the proposed unit cell is lower than that of the single-element unit cell, across the frequency range 6–7.5 GHz, which facilitates better impedance matching between the absorber and air. The proposed four-element unit cell exhibits a right shift in resonance frequency in comparison to the single-element unit cell. The resonance frequency is affected in particular by the spacing between the elements and other geometric parameters. The characteristic of these unit cells is changing mainly due to the changes in reactance of the structure and coupling between adjacent elements. Inter-element spacing causes capacitive coupling, which increases the impedance of the absorber and provides better matching with the intrinsic impedance of air. The unit cell having single-element exhibits S_{11} values above −10 dB from 6.7 to 7.2 GHz, as shown in Fig. 4*a*. Hence the proposed four-element unit cell offers higher absorption across the frequency range of 6.2–7.5 GHz in comparison to the single-element unit cell, as shown in Fig. 4*b*. Further, the single-element unit cell exhibits <90% absorption in the frequency range of 6.7–7.2 GHz. Therefore, when a 2 × 2 array (quad-element) is used as the element of the unit cell, better response in reflection coefficient and absorption characteristics are obtained across the frequency range of 4.9–7.5 GHz than that of the 1-element and 16-element unit cell. As we are more concerned about the absorption performance rather than the size of the unit cell, therefore, the four-element unit cell is preferred over the single-element unit cell. Since the proposed unit cell dimension is only $0.13\lambda \times 0.13\lambda$, it is compact and can be a promising candidate for designing a wideband absorber. One can also consider the single-element unit cell if the space requirement is a more important factor for the corresponding applications.

The proposed absorber exhibits three resonances at 5.2, 6.1 and 7.4 GHz. It is well known that at least one resonance (electric or magnetic) should be provided by the structure for absorption [2].

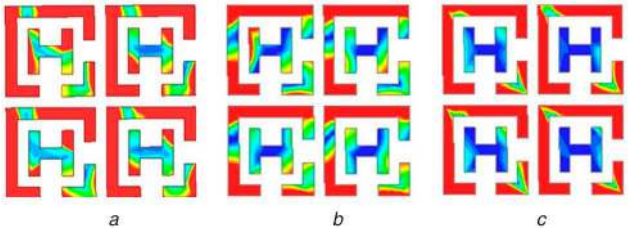

Fig. 5 *E-field distribution at*
(a) 7.4 GHz, ***(b)*** 6.1 GHz, ***(c)*** 5.2 GHz
Red indicates maximum and blue indicates minimum of the *E*-field

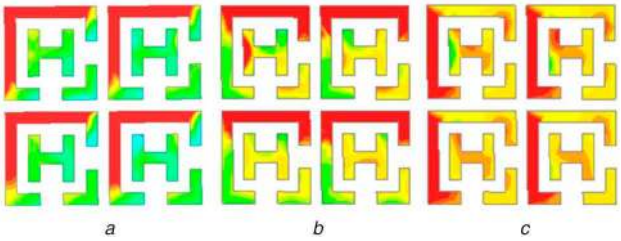

Fig. 6 *H-field distribution at*
(a) 7.4 GHz, ***(b)*** 6.1 GHz, ***(c)*** 5.2 GHz
Red indicates maximum and blue indicates minimum of the *H*-field

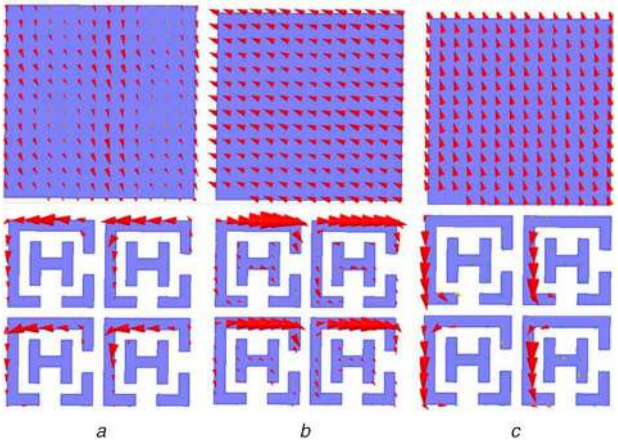

Fig. 7 *Top: current distributions on ground surface; bottom: current distributions on top layers*
(a) 7.4 GHz, ***(b)*** 6.1 GHz, ***(c)*** 5.2 GHz

Figs. 5 and 6 show the electric and magnetic field distributions, respectively, on the absorber at the resonance frequencies.

At 7.4 GHz, electric fields are higher suggesting the electrical resonance. A high density of the electric field around the ring resonator (except the gap area) and a low density around the dog-bone-shaped structure are detected. The electric field is strongly coupled on the ring resonator and gives an electrical response at this resonance frequency. The surface charges, which are induced by the strong electric fields around the resonators, produce surface currents responsible for the resonances and resonant absorption. Magnetic fields are higher at 5.2 and 6.1 GHz resulting in magnetic resonance due to surface charge inductions. As seen from the current distribution in Fig. 7, parallel currents in the top and ground layers excite electric resonance at 7.4 GHz, whereas the circulating anti-parallel currents in the top and ground layers induced by the incident time-varying magnetic field excite magnetic resonances at 5.2 and 6.1 GHz. Since the direction of current is the same in the adjacent metallic conductors in Fig. 7, it can be inferred that there exists inductive coupling impedance, which is responsible for absorption.

At 5.2 and 6.1 GHz, parallel currents in the first and second layers contribute to the inductive effect. At 7.4 GHz, antiparallel currents in the first and second layers contribute to the capacitive effect. The resonant frequency is mainly controlled by the dimensions of the split-ring resonators, and the metallic back layer

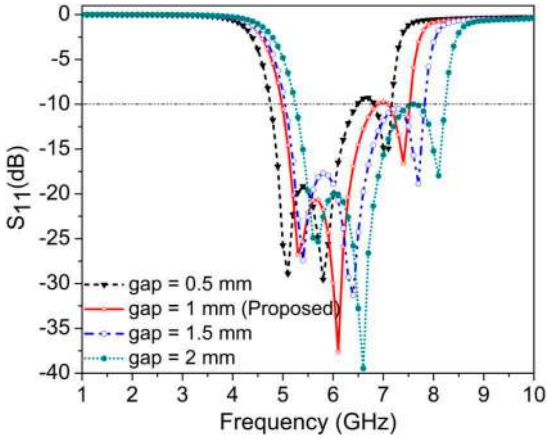

Fig. 8 *Variation of gap width in the square loop resonator*

also supports the resonance. Dimensions of the proposed model are tuned to increase the resonance, and it can be seen that the gaps in the ring resonator structure are created for this purpose. As observed in Fig. 8, with the increase of gap width in the square loop metallic structure in both the layers, the capacitance decreases which leads to increase in the resonance frequency. The gap width is finalised to 1 mm for the proposed design. If the gap width is increased to 1.5 mm, the electrical length of the path traversed by current decreases which shift the resonance frequency towards the right. On the contrary, when the gap width is 0.5 mm, the electrical path length traversed by current increases, thereby decreasing the resonance frequency.

The absorption characteristics are dependent on the thickness of the absorber. The minimum thickness (t) of the absorber can be found in [22] as given in (1):

$$t \geq \frac{\int_{-\infty}^{+\infty} \ln\left(\tau(\lambda)\right) \mathrm{d}\lambda}{2 * (\pi) * (\Pi)} \tag{1}$$

where n is the refractive index and τ is the reflection coefficient.

When the distance between the front and back sides is increased, the resonances become weaker due to lower mutual coupling. Hence, the thickness of the dielectric slab must be selected optimally to provide strong resonances:

$$A(\omega) = 1 - |S_{11}(\omega)|^2 - |S_{21}(\omega)|^2 \tag{2}$$

The absorptivity $A(\omega)$ can be found from (2) where $|S_{11}(\omega)|^2$ is the reflected power and $|S_{21}(\omega)|^2$ is the transmitted power of the incident EM radiation at angular frequency ω. As the proposed structure is completely laminated by the copper at the bottom layer, so $S_{21}(\omega) = 0$, hence, $A(\omega) = 1 - |S_{11}(\omega)|^2$.

Due to mutual coupling between the top and the bottom FSS layers, admittance matching occurs at resonance condition, which restrains the incident waves in the absorber, thus aiding absorption. The normalised impedance (Z) can be computed from S-parameters [5] as given in (3):

$$Z = \frac{\sqrt{(1 + S_{11})^2 - S_{21}^2}}{\sqrt{(1 - S_{11})^2 - S_{21}^2}} \tag{3}$$

As observed in Fig. 9, from 5.5 to 7.5 GHz the imaginary part of effective impedance (Z) is nearly 0. The real part of normalised impedance is close to 1 because it is matched with the intrinsic impedance (377 Ω) of air across the same operating band.

The refractive index (n) can be retrieved [5] by applying S-parameters and normalised impedance (Z) of (3) in (4):

$$\mathrm{j} = \frac{S_{21}}{1 - (S_{11}(Z - 1)/(Z + 1))} \tag{4}$$

where k is the phase constant.

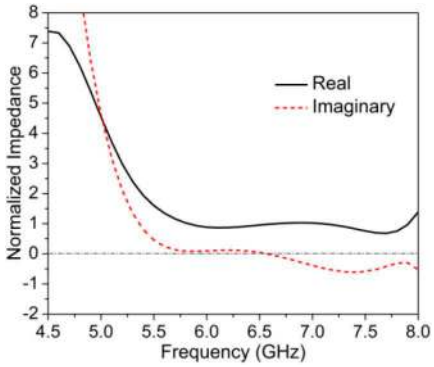

Fig. 9 *Normalised impedance of the absorber*

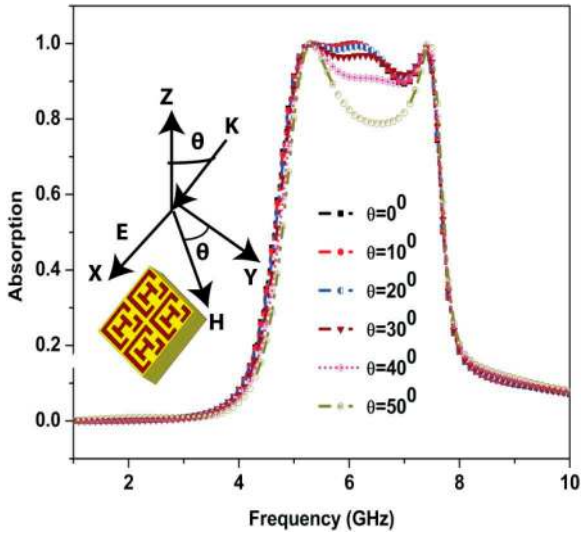

Fig. 10 *Angular stability in absorption characteristics under TE mode*

The large imaginary part of the refractive index ensures high relative permittivity. This suggests that the EM wave gets attenuated while propagating inside the absorber. Maximum absorption of 99.98% is observed at the resonant frequency of 6.1 GHz. The unit cell exhibits great angular stability for both TE and TM mode oblique incidences up to 50° beyond which there is a degradation of absorption characteristics, as shown in Figs. 10 and 11, respectively. The geometrical dimensions are parametrically optimised to obtain maximum absorption at the operating frequencies. To achieve perfect absorption with near-zero reflection, the effective permittivity (ε_{eff}) and permeability (μ_{eff}) can be manipulated to have the same value for effective impedance matching over the frequency spectrum. This can be accomplished by properly tuning incident electric and magnetic field responses for providing perfect absorption. The absorber absorbs out-of-band co-polarised waves which enhance the reduction of the out-of-band co-polarised RCS.

3 Equivalent circuit model (ECM) of the proposed absorber

In this section, an equivalent circuit of the proposed absorber is developed, analysed and validated. The four dog-bone-shaped resonators are modelled as an equivalent parallel circuit comprising an inductance (L) and capacitance (C) while outer split-ring square loop resonators are modelled as an equivalent series circuit comprising an inductance ($L1$) and capacitance ($C1$). The inductance is due to the square loop element. The gap in the split-ring resonator contributes to capacitance. The unit cell comprises four split-ring square loop resonators. Hence four series LC circuits are considered to be parallel with each other, as shown in Fig. 12. The metallic plate backed FR4 substrate is modelled as a shorted transmission line. The characteristic impedance of the transmission line which models the wave propagation in the substrate is given

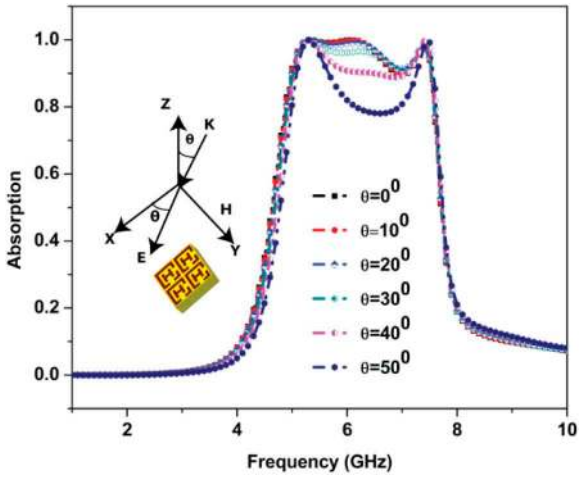

Fig. 11 *Angular stability in absorption characteristics under TM mode*

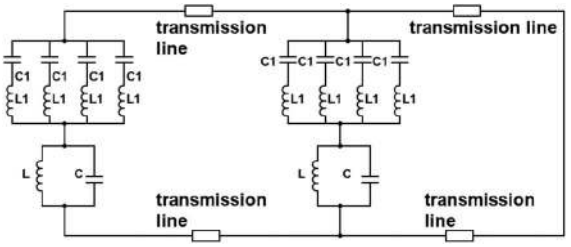

Fig. 12 *Equivalent circuit of the absorber unit cell*

by $Z_0/\sqrt{\varepsilon_r}$, where $Z_0 = 377\ \Omega$. The short-circuited transmission line section resonates at a frequency corresponding to $\lambda/4\sqrt{\varepsilon_r}$ giving zero admittance. The substrate thickness is 1.6 mm which corresponds to a quarter wavelength at resonating frequency 5.6 GHz. Hence minimum return loss occurs at 5.2 GHz as observed from the absorption characteristics. For the shorted transmission line of length l, the input impedance Z_T is given by (5):

$$Z_T = jZ_l\tan(\beta l) \tag{5}$$

Z_T = infinity when $\beta l = \pi/2$. The S_{11} parameter is derived from the circuit elements using (6– (16):

$$Z_l = \frac{Z_0}{\sqrt{\varepsilon_r}} = 179.83\,\Omega$$

For lossless transmission

$$Z_{lTE} = \frac{\omega\mu_r\varepsilon_r}{\beta} \text{ and } Z_{lTM} = \frac{\beta}{\omega\varepsilon_0\mu_r} \tag{6}$$

$$Z_2 = j\omega L1 + \frac{1}{j\omega C1} \tag{7}$$

The impedance equivalent of four parallel arms = $Z_2/4$:

$$Z_3 = \frac{j\omega L}{1-\omega^2 LC} \tag{8}$$

The total impedance of the first shunt arm:

$$Z_4 = \frac{Z_2}{4} + Z_3 \tag{9}$$

$$Z_5 = \frac{Z_4 Z_T}{Z_4 + Z_T} \tag{10}$$

Z_5 behaves as a load to the transmission line:

$$Z_{in} = \frac{Z_1(Z_5 + \mathrm{j}\, Z_1 \tan \beta l)}{(Z_1 + \mathrm{j}\, Z_5 \tan \beta l)} \tag{11}$$

The net input impedance:

$$Z_i = \frac{Z_{in} Z_4}{Z_{in} + Z_4} \tag{12}$$

$$\Gamma(\text{Reflectioncoefficient}) = \frac{Z_1 - Z_0}{Z_1 + Z_0}$$

The *ABCD* matrix of the absorber

$$= \begin{bmatrix} 1 & 0 \\ \frac{1}{Z_4} & 1 \end{bmatrix} \begin{bmatrix} \cos\theta & \mathrm{j}Z_1 \sin\theta \\ \frac{\mathrm{j}\sin\theta}{Z_1} & \cos\theta \end{bmatrix} \begin{bmatrix} 1 & 0 \\ \frac{1}{Z_4} & 1 \end{bmatrix} \begin{bmatrix} 1 & 0 \\ \frac{1}{\mathrm{j}Z_1 \tan\theta} & 1 \end{bmatrix} \tag{13}$$

it can be further simplified to $\begin{bmatrix} A & B \\ C & D \end{bmatrix} =$

$$\begin{bmatrix} 2\cos\theta + \mathrm{j}\sin\theta & \mathrm{j}Z_1 \sin\theta \\ \cos\theta\left(\frac{1}{Z_1} + \frac{2}{Z_4}\right) + \mathrm{j}\sin\theta\left(\frac{1}{Z_4} + \frac{1}{Z_1}\right) & \cos\theta + \mathrm{j}\left(\frac{Z_1 \sin\theta}{Z_4}\right) \end{bmatrix}$$

θ is the electrical length of the transmission line.

At resonance, $\theta = \Pi/2$ as the length of the transmission line is $\lambda/4$.

The *ABCD* parameters in (14) are used for obtaining the reflection coefficient in (15):

$$\begin{bmatrix} A & B \\ C & D \end{bmatrix} = \begin{bmatrix} \mathrm{j} & \mathrm{j}Z_1 \\ \mathrm{j}\left(\frac{1}{Z_4} + \frac{1}{Z_4}\right) & \mathrm{j}\frac{Z_1}{Z_4} \end{bmatrix} \tag{14}$$

$$S_{11} = \frac{A + (B/Z_0) - CZ_0 - D}{A + (B/Z_0) + CZ_0 + D} \tag{15}$$

Substituting the values of A, B, C, and D in (15) we get

$$S_{11} = \frac{1 + (Z_1/Z_0) - Z_0((1/Z_4) + (1/Z_1)) - (Z_1/Z_4)}{1 + (Z_1/Z_0) + Z_0((1/Z_4) + (1/Z_1)) + (Z_1/Z_4)} \tag{16}$$

where

$$Z_4 = \mathrm{j}\left(\frac{\omega L}{1 - \omega^2 LC} + \frac{\omega L1}{4} - \frac{1}{4\omega C1}\right)$$

S_{11} can, therefore, be computed if the lumped element values are known. The proposed circuit model (Fig. 12) is designed in the circuit simulator (ADS). The values of inductances and capacitances are obtained from circuit simulation in ADS such that the S_{11} characteristics in ADS closely follow the S_{11} characteristics as obtained from full-wave simulation (HFSS). For $L = 15$ nH, $C = 5$ pF, $L1 = 5$ nH, and $C1 = 20$ pF the ECM in ADS yields the closest result (S_{11}) to that obtained from HFSS simulation. The S_{11} responses as obtained from ADS and HFSS are in good agreement, as shown in Fig. 13 thus validates the proposed ECM. The 3D EM simulations in HFSS capture metal coupling in 3D but the planar structure simulated in ADS uses a 2D EM field solver which simulates structures with transverse electro-magnetic (TEM) wave propagation. In ADS, the values of equivalent lumped capacitors and inductors are optimised to match the *S*-parameters at the resonant frequencies only. The lumped component values vary along with frequency and hence a slight variation in the S_{11} characteristics is observed in the circuit simulation.

Now the constitutive parameters μ_r and ε_r of the proposed absorber are retrieved from the reflection coefficient, using (17)–(21) as described in [25]. The magnitude of S_{11} is a function of μ_r and ε_r as given in (17):

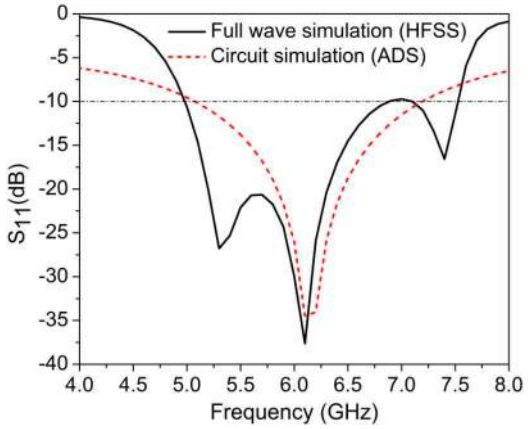

Fig. 13 *Comparison of circuit simulation and full-wave simulation*

$$\left|S_{11}\right| = \left|\frac{(\mu_r/\varepsilon_r) - 1}{(\mu_r/\varepsilon_r) + 1}\right| \tag{17}$$

where μ_r is the complex relative permeability and ε_r is the complex relative permittivity.

The attenuation factor α, which is a measure of dielectric loss in the substrate can be computed from μ_r and ε_r:

$$\alpha = \frac{\omega}{\sqrt{2c}} \frac{\sqrt{(\mu''\varepsilon'' - \mu'\varepsilon')(\mu'^2 + \mathrm{j}\,\varepsilon''2)}}{1} \tag{18}$$

where c is the speed of light.

$$\mu_r = \mu' - \mathrm{j}\mu'' \quad \text{and} \quad \varepsilon_r = \varepsilon' - \mathrm{j}\varepsilon''$$

$$\varepsilon^* = \frac{\gamma}{\gamma_0} \frac{(1 - \Gamma)}{(1 + \Gamma)} \tag{19a}$$

$$\mu^* = \frac{\gamma}{\gamma_0} \frac{(1 + \Gamma)}{(1 - \Gamma)} \tag{19b}$$

where

$$\gamma_0 = \frac{2\pi}{\lambda_0} \quad \text{and} \quad \Gamma = \frac{Z_n - 1}{Z_n + 1}$$

λ_0 is computed at the resonant frequency of 6.1 GHz. Z_n is the normalised input impedance of the absorber. The effective permittivity (ε_{eff}) and permeability (μ_{eff}) are extracted from the *S*-parameters using (20) and (21):

$$\varepsilon_{eff} = 1 + \frac{2\mathrm{j}\,(1 - S_{11})}{(k_0)\, h\, (1 + S_{11})} \tag{20}$$

$$\mu_{eff} = 1 + \frac{2\mathrm{j}\,(1 + S_{11})}{(k_0)\, h\, (1 - S_{11})} \tag{21}$$

where k_0 is the wave number of thefree space.

The effective permittivity and permeability can be adjusted independently by varying the dimensions of the unit cell to match the effective impedance of the metamaterial absorber with the free space impedance for achieving large resonant dissipation. Fig. 14 presents the variation of the real parts of both ε_{eff} and μ_{eff} across the absorption band. It establishes the fact that both electric and magnetic fields contribute to the absorption. Negative permittivity occurs at the higher frequencies due to electrical resonance at 7.4 GHz while negative permeability is observed at the lower frequencies due to magnetic resonances at 5.2 and 6.1 GHz. Also, at the highest analysed frequencies, the permittivity is negative and, thus, the induced electric field opposes the incident EM wave in this frequency range. At 6.1 GHz, EM wave reflection is minimised by proper matching between ε_{eff} and μ_{eff}.

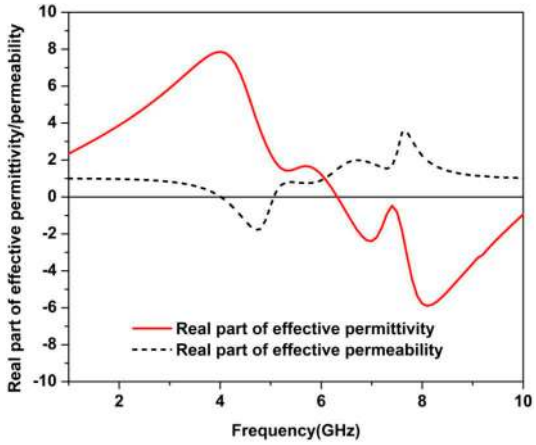

Fig. 14 *Variation of real part of effective permittivity and permeability*

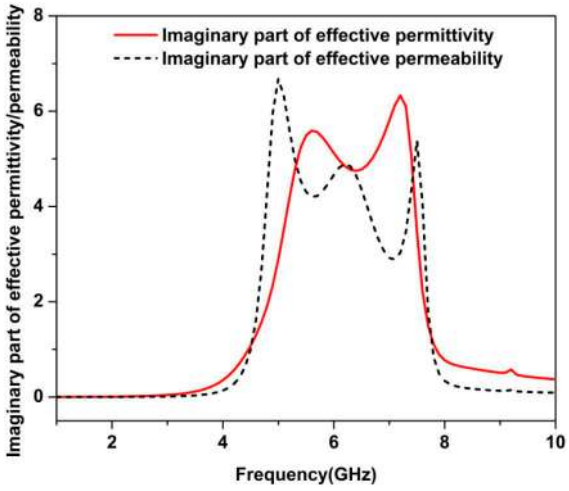

Fig. 15 *Variation of imaginary part of effective permittivity and permeability*

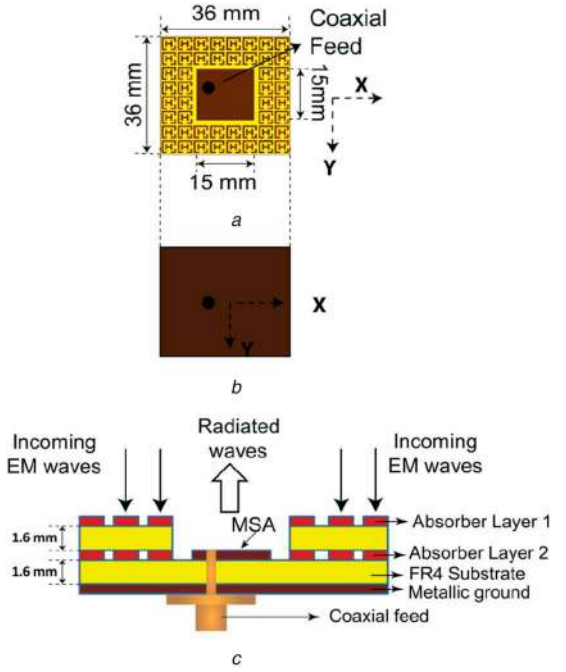

Fig. 16 *Structure of the absorber integrated MSA*
(a) Top view, ***(b)*** Bottom view, ***(c)*** Side view of composite structure

The imaginary parts of the constitutive parameters are accountable for the losses. The positive curves (Fig. 15) of both imaginary parts of ε_{eff} and μ_{eff} indicate that losses occur in the

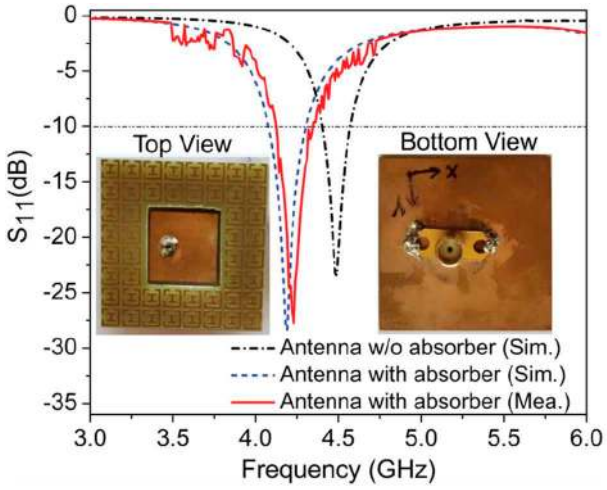

Fig. 17 *Simulated and measured S_{11} plots of different structures*

metamaterial. Therefore, the proposed absorber is driven by both electric and magnetic fields. The imaginary part of complex permittivity indicates the ohmic loss and represents the energy dissipated as heat and dielectric leakage due to variation of ac electric field in the dielectric material. The imaginary part of the complex permeability provides a measure of resistive loss. The high positive value of constitutive parameters in Fig. 15 indicates high resistive loss which leads to high absorption in the operating band.

4 Integration of square patch antenna with proposed absorber

Initially, a conventional square patch (15 mm × 15 mm) is designed on an FR4 substrate of thickness 1.6 mm with a ground plane dimension of 36 mm × 36 mm to operate at 4.2 GHz, which is within the negative permeability region of the proposed absorber. Now, for the purpose of RCS reduction, the proposed absorber structure is also realised along with this MSA structure. The ground plane of MSA serves as the metallic back of the absorber. Two FR4 sheets (36 mm × 36 mm) of thickness 1.6 mm are sandwiched back to back with proper alignment to realise the composite structure of the proposed design for lower RCS, as shown in Fig. 16. The proposed square patch is printed on the top side of the lower FR4 sheet. Now top two layers of the proposed absorber are printed on both sides of the upper FR4 sheet in a square (36 mm × 36 mm) annular ring (of width 17 mm) form to surround the square patch. In order to lead EM waves to radiate into the outer space as much as possible and to reduce the coupling between the absorber and the patch, a gap of 2 mm is kept between them. An air gap of 1.6 mm exists above the antenna which reduces the reflections of the impinging EM waves due to low permittivity of air. Fig. 17 shows that with the absorber, the antenna exhibits lower reflection coefficients, which ensure better matching. In higher frequency band 4.9–7.5 GHz, all the incoming EM waves are absorbed by the FSS cells encompassing the antenna thus reducing reflections. The photos of the fabricated prototype are also shown in the inset of Fig. 17. The reduction of scattered power reduces both the monostatic and bistatic RCS of the structure. When the MSA is 3.2 mm thick and is coplanar with the absorber, the RCS increases due to the reflection of EM waves from the antenna surface due to higher permittivity. A greater RCS reduction is observed for 1.6 mm thick MSA as compared to the MSA with 3.2 mm thickness, as shown in Fig. 18. RCS of the absorber integrated antenna varies with change in the angle of incidence. With the increase of angle of incidence from 0° to 50°, monostatic RCS of the absorber integrated antenna falls as evident from Fig. 19. At 6.2 GHz, a maximum of 14.73 dB RCS reduction is exhibited for 20° angle of incidence while a maximum of 11 and 8 dB RCS reduction takes place for 40° and 50° off-normal incidence at 6.5 GHz when compared with MSA.

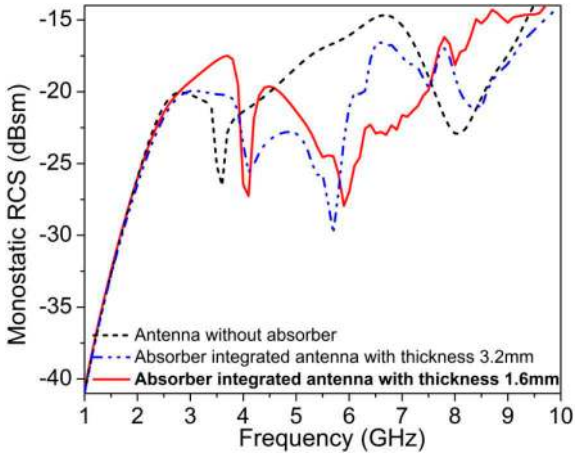

Fig. 18 *Comparison of monostatic RCS reduction of integrated antenna of different thickness*

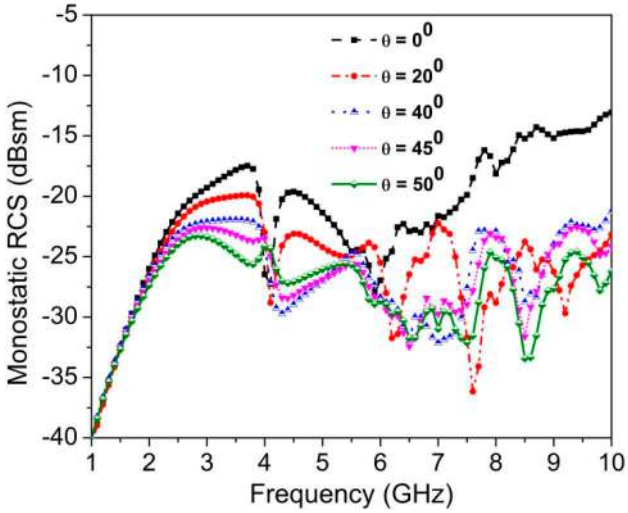

Fig. 19 *RCS reduction of the antenna for oblique incidence*

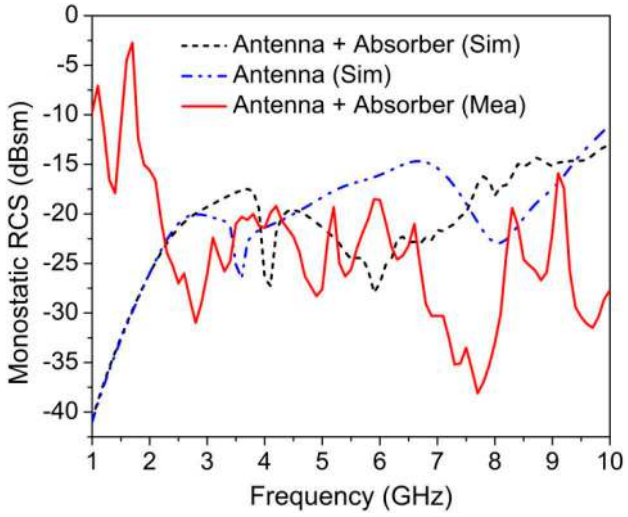

Fig. 20 *Simulated and measured monostatic RCS reduction of antenna with and without absorber*

5 Results and discussion

In Fig. 20, the measured monostatic RCS of the absorber integrated MSA undergoes a maximum reduction of 15 dB in the frequency range of 4–8 GHz as against 12 dB when simulated in the frequency range of 4.5–7.5 GHz in comparison to the conventional MSA alone. A slight mismatch in the simulated and measured results is attributed to the error in the fabrication and measurement process. The results of bistatic RCS at 5.8 GHz in Fig. 21

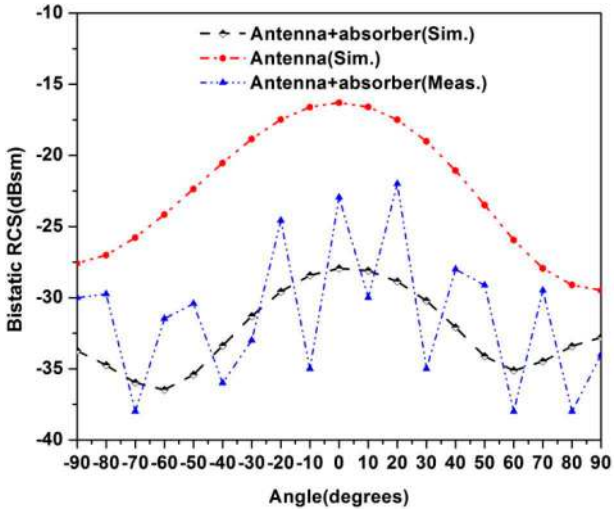

Fig. 21 *Simulated and measured bistatic RCS reduction of antenna with and without absorber*

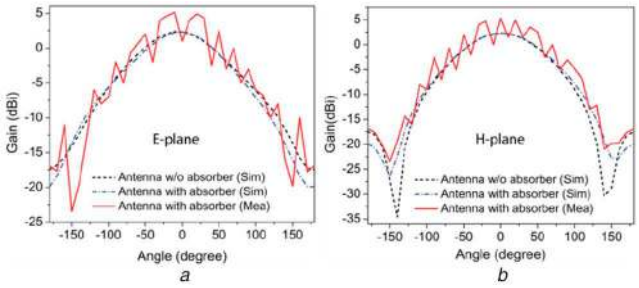

Fig. 22 *Simulated and measured co-polarised radiation patterns of the antenna with and without absorber in*
(a) *E*-plane, ***(b)*** *H*-plane

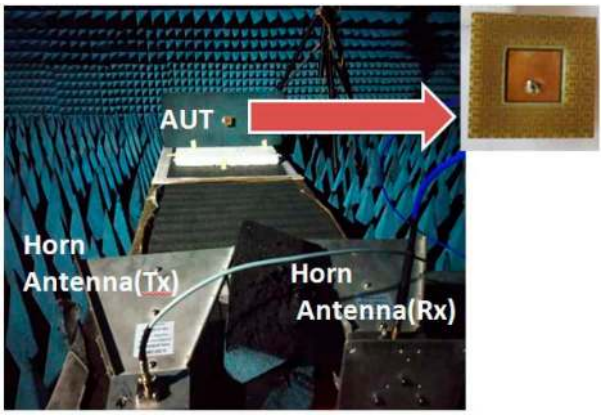

Fig. 23 *RCS measurement set-up in the anechoic chamber*

demonstrate that the absorber is effective for RCS reduction of MSA from −90° to +90°, and also simultaneously verify that the incident wave is not scattered in any other direction. The simulated and measured *E*-plane and *H*-plane radiation patterns of the antenna are shown in Fig. 22. It is observed that the co-polarised radiation characteristics of the antenna are not perturbed by the absorber. However, it reduces the RCS effectively over the antenna operating band as well as out of the operating band. The simulated peak gain of the MSA with and without absorber is 2.31 and 2.33 dBi, respectively. The RCS measurement set-up is created in a microwave anechoic chamber as shown in Fig. 23.

In Table 1, a comparison of the proposed work is made with previous works. Although RCS reduction is obtained over a wider bandwidth, angular stability is low in [6]. Similarly, the angular stability is higher in [5] but scores low in RCS reduction bandwidth. A higher RCS reduction bandwidth is achieved in [11] at the cost of increased unit cell dimensions. Higher angular

Table 1 Comparison with previous works

Ref.	RCS reduction, dB	RCS reduction band, GHz	Unit cell size	Angular stability
[5]	14	5.46–5.68	$0.164\lambda \times 0.164\lambda$	60°
[6]	14	2–12	$0.06\lambda \times 0.04\lambda$	30°
[10]	10.07	1–13	$0.04\lambda \times 0.04\lambda$	not mentioned
[11]	10	3–9.2	$0.36\lambda \times 0.29\lambda$	45°
this work	15	4–8	$0.135\lambda \times 0.135\lambda$	50°

stability and compactness of the proposed absorber are thus considered to be superior to the existing works.

6 Conclusion

A thin FSS-based metal printed and metallic backed absorber without using resistive surface and lumped resistors has been presented for the RCS reduction of an MSA. This low-cost easy-to-fabricate absorber can absorb the out-of-band (4.5–7.5 GHz) incident EM waves effectively. Conceiving the top two layers of the absorber in a square-shaped annular ring embedded with dog-bone structure, and using the full metallic ground plane of the MSA as the back metal plate of the absorber are the key features of this proposed composite design. The integration of this proposed absorber reduces the monostatic and bistatic RCS of the MSA significantly without perturbing the radiation performance of the antenna. Hence, this proposed composite structure is suitable for the stealth technology.

7 Acknowledgment

The authors would like to acknowledge Prof. Kumar Vaibhav Srivastava of IIT Kanpur, India for providing their measurement facilities.

8 References

[1] Zeng, X., Gao, M., Zhang, L., *et al.*: 'Design of a triple-band metamaterial absorber using equivalent circuit model and interference theory', *Microw. Opt. Technol. Lett.*, 2018, **60**, (7), pp. 1585–1835

[2] Jiang, H., Xue, Z., Li, W., *et al.*: 'Multiband polarisation insensitive metamaterial absorber based on circular fractal structure', *IET Microw. Antennas Propag.*, 2016, **10**, (11), pp. 1141–1145

[3] Li, S.-J., Cao, X.-Y., Gao, J., *et al.*: 'Analysis and design of three layers perfect metamaterial-inspired absorber based on double split-serration-rings structure', *IEEE Trans. Antennas Propag.*, 2015, **63**, (11), pp. 5155–5160

[4] Sim, M.S., You, K.Y., Esa, F., *et al.*: 'Multiband metamaterial microwave absorbers using split ring and multiwidth slot structure', *Int. J. RF Microw. Comput. Aided Eng.*, 2018, **28**, (7), pp. 1–13

[5] Liu, T., Cao, X., Gao, J., *et al.*: 'RCS reduction of waveguide slot antenna with metamaterial absorber', *IEEE Trans. Antennas Propag.*, 2013, **61**, (3), pp. 1479–1484

[6] Liu, Y., Hao, Y., Li, K., *et al.*: 'Radar cross section reduction of a microstrip antenna based on polarization conversion metamaterial', *IEEE Antennas Wirel. Propag. Lett.'*, 2016, **15**, pp. 80–83

[7] Kundu, D., Mohan, A., Chakrabarty, A.: 'Single layer wideband microwave absorber using array of crossed dipoles', *IEEE Antennas Wirel. Propag. Lett.*, 2016, **15**, pp. 1589–1592

[8] Yang, J., Shen, Z.: 'A thin and broadband absorber using double-square loops', *IEEE Antennas Wirel. Propag. Lett.*, 2007, **6**, pp. 388–391

[9] Xie, D., Liu, X., Guo, H., *et al.*: 'Wideband absorber with multi-resonant gridded-square FSS for antenna RCS reduction', *IEEE Antennas Wirel. Propag. Lett.*, 2017, **16**, pp. 629–632

[10] Xue, J., Jiang, W., Gong, S.: 'Wideband RCS reduction of microstrip antenna based on 2.5-dimension miniaturized frequency selective surface'. IEEE 5th Asia-Pacific Conf. on Antennas and Propagation (APCAP), Kaohsiung, 2016, pp. 209–210

[11] Chen, Q., Fu, Y.: 'A planar stealthy antenna radome using absorptive frequency selective surface', *Microw. Opt. Technol. Lett.*, 2014, **56**, (8), pp. 1788–1792

[12] Ma, S., Hou, X., Zhang, Q., *et al.*: 'Ultrawideband metamaterial absorber using three layer ring and patch resonators'. IEEE MTT-S Int. Wireless Symp.,(IWS), Chengdu, China, 2018

[13] Ze, Y., Zhen, L.G.: 'An ultra-thin and broadband absorber using slotted metal loop with multi layers', *Optik*, 2016, **127**, pp. 387–389

[14] Winson, D., Choudhury, B., Kumar, N.S., *et al.*: 'Design and development of a hybrid broadband radar absorber using metamaterial and graphene', *IEEE Trans. Antennas Propag.*, 2019, **67**, (8), pp. 5446–5452

[15] Yu, W., Luo, G.Q., Yu, Y., *et al.*: 'Dual-polarized band-absorptive frequency selective rasorber using meander-line and lumped resistors', *IEEE Trans. Antennas Propag.*, 2019, **67**, (2), pp. 1318–1322

[16] Lin, C.W., Shen, C.-K., Wu, T.-L.: 'Ultracompact via-based absorptive frequency-selective surface for 5-GHz Wi-Fi with passbands and high-performance stability', *IEEE Trans. Compon. Packag. Manuf. Technol.*, 2018, **8**, (1), pp. 41–49

[17] Ikegami, T., Sakakibara, K., Nomoto, G., *et al.*: 'Design of frequency selective surface by matrix transformation of layer structure to reduce return loss of thick dielectric plate'. Proc. of IEEE CAMA (Conf. on Antenna Measurements and Applications, Tsukuba, 2017, pp. 182–185

[18] Silva, M.W.B., Araujo, H.X., Campos, A.L.P.S.: 'Design of a narrow band and wideband absorbers using resistive FSS concept for the X and Ku band application', *Microw. Opt. Technol. Lett.*, 2018, **60**, (9), pp. 2128–2132

[19] Wan, D., Bie, S., Zhou, J., *et al.*: 'A thin and broadband microwave absorber based on magnetic sheets and resistive FSS', *Progr. Electromagn. Res. C*, 2015, **56**, pp. 93–100

[20] Lin, C.-W., Shen, C.-K., Chiu, C.-N., *et al.*: 'Design and modeling of a compact partially transmissible resistor-free absorptive frequency selective surface for Wi-Fi applications', *IEEE Trans. Antennas Propag.*, 2019, **67**, (2), pp. 1306–1311

[21] Yoo, M., Lim, S., 'Polarization-independent and ultrawideband metamaterial absorber using a hexagonal artificial impedance surface and a resistor-capacitor layer', *IEEE Trans. Antennas Propag.*, 2014, **62**, (5), pp. 2652–2658

[22] Shang, Y., Shen, Z., Xiao, S.: 'On the design of single-layer circuit analog absorber using double-square-loop array', *IEEE Trans. Antennas and Propag.*, 2013, **61**, (12), pp. 6022–6029

[23] Ghosh, S., Bhattacharyya, S., Srivastava, K.V.: 'Bandwidth-enhancement of an ultrathin polarization insensitive metamaterial absorber', *Microw. Opt. Technol. Lett.*, 2014, **56**, (2), pp. 350–355

[24] Sohrab, A.P., Atlasbaf, Z.: 'A circuit analog absorber with optimum thickness and response in X-band', *IEEE Antennas Wirel. Propag. Lett.*, 2013, **12**, pp. 276–279

[25] Aráujo, B., Siqueira, G., Kemptner, E., *et al.*: 'An ultrathin and ultrawideband metamaterial absorber and an equivalent-circuit parameter retrieval method', *IEEE Trans. Antennas Propag.*, 2020, **68**, pp. 3739–3746 (doi: 10.1109/tap.2020.2963900)